metals

MDPI

Article

Microstructural Evolution during Pressureless Sintering of Blended Elemental Ti-Al-V-Fe Titanium Alloys from Fine Hydrogenated-Dehydrogenated Titanium Powder

Changzhou Yu, Peng Cao * and Mark Ian Jones *

Department of Chemical and Materials Engineering, The University of Auckland, Private Bag 92019, Auckland 1142, New Zealand; cyu060@aucklanduni.ac.nz

* Correspondences: p.cao@auckland.ac.nz (P.C.); mark.jones@auckland.ac.nz (M.I.J.); Tel.: +64-9-9236924 (P.C.); +64-9-9234548 (M.I.J.)

Received: 10 June 2017; Accepted: 24 July 2017; Published: 26 July 2017

Abstract: A comprehensive study was conducted on microstructural evolution of sintered Ti-Al-V-Fe titanium alloys utilizing very fine hydrogenation-dehydrogenation (HDH) titanium powder with a median particle size of 8.84 μm. Both micropores (5–15 μm) and macropores (50–200 μm) were identified in sintered titanium alloys. Spherical micropores were observed in Ti-6Al-4V sintered with fine Ti at the lowest temperature of 1150 °C. The addition of iron can help reduce microporosity and improve microstructural and compositional homogenization. A theoretical calculation of evaporation based on the Miedema model and Langmuir equation indicates that the evaporation of aluminum could be responsible for the formation of the macropores. Although reasonable densification was achieved at low sintering temperatures (93–96% relative density) the samples had poor mechanical properties due mainly to the presence of the macroporosity and the high inherent oxygen content in the as-received fine powders.

Keywords: titanium alloys; sintering; powder metallurgy; microstructural evolution

1. Introduction

Sintering is by far the most common consolidation method in titanium powder metallurgy. The initial stage of sintering can be empirically modeled in terms of isothermal neck growth as measured by the neck size ratio X/D [1]:

$$(X/D)^n = Bt/D^m \quad (1)$$

where D is the particle diameter, X = neck diameter, t = isothermal sintering time, and B is a collection of material and geometric constants. The values of n, m, B depend on the mechanism of mass transport. The above empirical equation indicates that sintering is highly sensitive to the particle size, with a smaller particle size giving rise to more rapid densification.

The sintering data compiled by Robertson et al. confirms that a finer particle size is beneficial for titanium powder densification [2]. However titanium powders with very fine particle size are not usually available, particularly if a low impurity level is required. A particle size of −100 mesh (<150 μm), −200 mesh (<75 μm), or −325 mesh (<45 μm), is most commonly used [3–5]. A recent study reports a novel technique to produce titanium powder with a mean particle size of <10 μm [6]. However, the powder reported has a high impurity content of oxygen (>0.8 wt %) [6]. It is known that high oxygen content can adversely affect mechanical properties, especially ductility [4,5,7], and therefore the aim of this research is primarily to investigate the feasibility of using a very fine titanium powder

to sinter titanium products and investigate the effects of these fine powders on densification. Ti-6Al-4V is known as a "work-horse" α + β titanium alloy, which has high strength and good ductility. However, the β-stabilizing element vanadium is not only expensive but also toxic to human beings if used as an implant [8]. For blended elemental sintering of Ti-6Al-4V, better sinterability can be obtained using a master alloy powder (Al-V) than when using elemental aluminum and vanadium [9]. Our first objective of this work was to investigate the sinterability of Ti-6Al-4V by using fine titanium powder and Al-V master alloy powder (60 wt % Al, 40 wt % V).

Current titanium powder metallurgy research has been largely devoted to cost reduction in titanium components by both developing cost-effective powder manufacturing and developing low-cost titanium alloys [10–12]. In the development of low-cost titanium alloys, the introduction of iron (Fe) as a β-Ti stabilizer into the alloy compositions has been widely explored for powder metallurgical titanium alloys [13,14].

Iron is much cheaper than titanium, and the application of 5% Fe is equivalent to saving the use of 5% Ti [15,16]. The sinterability of titanium alloys can be enhanced by the addition of iron since the mobility of titanium atoms is accelerated by the rapid diffusion of iron [13,17,18]. The fast diffusion of iron in titanium alloy is evidenced by the fact that iron is essentially uniform in a blended elemental Ti-10V-2Fe-3Al alloy when heated at 5 °C/min to 1200 °C [19]. Ti-10V-2Fe-3Al (O $\leq$ 0.13; N $\leq$ 0.05; C $\leq$ 0.05; H $\leq$ 0.015; all in wt %), assigned formally as TIMETAL® 10-2-3, has been realized for aircraft under-carriage applications [14,19]. Further experiments indicate that the enhancement in sinterability observed through the addition of fine iron powder (mean particle size = 8 μm) is not seen when working with coarser iron powder (mean particle size = 97 μm) [20].

Iron is a strong β phase stabilizer and suppresses the formation of the α phase and the eutectoid transformation β → α + TiFe when it cools below 595 °C, thus avoiding the formation of the brittle TiFe phase [21]. Such a phenomenon is also observed and validated by the recent research works conducted by Bolzoni et al. [11,12]. In addition to the fast diffusion mobility, iron additions also change the sequence of chemical homogenization for other alloying elements such as Al, V [14]. In another study, Yang et al. found a linear drop in ductility in Ti-xFe-0.5Si alloys with increasing Fe content from 3% to 6%. Such ductility drop is largely because the α-Ti phase becomes thinner and more acicular with increasing Fe [22].

The second objective of this work was to investigate the sintering behavior of low-cost Ti-Al-V-Fe titanium alloys with fine particle titanium powders through varying the amount of expensive master 60Al-40V powder and low-cost iron powder. The effect of the master alloy powder during sintering on sinterability is also discussed.

2. Experimental Procedures

2.1. Materials

The starting material for these experiments was a fine Ti powder produced from Ti sponge fines which were hydrogenated at 700 °C with a holding time of 2 h followed by 5 h ball milling. In this way, fine titanium hydride was produced with a median particle size <3 μm. An inhibitor (NaCl) was introduced for the coating of titanium hydride powder, which was further dehydrogenated at 630 °C for 2 h. The fine hydrogenation-dehydrogenation (HDH) titanium powders were water-leached by deionized water in order to remove the inhibitor. The median particle size was <10 μm. More detailed description of the fine Ti production process can be seen in the literature [6].

The fine titanium powder (O: 0.82 wt %, C: 0.058 wt %, H: 0.414 wt %, N: 0.575 wt %) was utilized to investigate the interaction effect of fine particle size and high impurity content on sintering and densification, with the understanding that the high impurity content of this powder may not result in outstanding mechanical properties. A commercially available 60Al-40V master alloy powder (−120 mesh; O: 0.18 wt %, C: 0.029 wt %, H: 0.0005 wt %, N: 0.16 wt %) and iron powder (−300 mesh; O: 0.67 wt %, C: 0.041 wt %, H: 0.0022 wt %, N: 0.262 wt %) supplied by Beijing Youxinglian Nonferrous

Metals Co. Ltd., Beijing, China, was employed to balance the designed alloy composition into Ti (0.6Al-0.4V)$_{10-x}$Fe$_x$, where x = 0, 2, 4, and 6. i.e., the Fe content ranged from 0 to 6 wt % as a replacement for the master alloy in a Ti-6Al-4V composition. The effect of beta stabilizing elements is generally quantified by an equivalent molybdenum (Mo), as given by:

$$(\text{Mo})_{\text{eq}} = \begin{array}{l}(\text{Mo}) + 0.67\ (\text{V}) + 0.44\ (\text{W}) + 0.28\ (\text{Nb}) + 0.22\ (\text{Ta}) + \\ 2.9\ (\text{Fe}) + 1.6\ (\text{Cr}) + 1.25\ (\text{Ni}) + 1.7\ (\text{Mn}) + 1.7\ (\text{Co}) - 1.0\ (\text{Al})\end{array} \quad (2)$$

The calculated equivalent Mo values for the Ti-4.8Al-3.2V-2Fe, Ti-3.6Al-2.4V-4Fe, and Ti-2.4Al-1.6V-6Fe are 3.1, 9.6, and 16 respectively. As such the Ti-4.8Al-3.2V-2Fe and Ti-3.6Al-2.4V-4Fe can be regarded α/β alloys while the Ti-2.4Al-1.6V-6Fe is a metastable β alloy.

2.2. Press-and-Sinter

Compacts were uniaxially pressed at a constant pressure of 300 MPa into two different cylindrical sizes: 16 mm diameter with 5–6 mm thickness, and 45 mm diameter with 3–4 mm thickness. No lubricants were added in the powder mixture, or applied on the die walls. The green density for all four alloys was 62.9 ± 0.5%. Compacts with dia = 16 mm were used for sintering densification calculations and the dia = 45 mm samples were sintered for tensile testing. Vacuum sintering (vacuum level: 2×10^{-3} Pa) was conducted in a high-temperature Mo-heating-element furnace (Dingli, Changsha, China) at 1150, 1250, and 1350 °C with a soaking time of 3 h. The racking material was molybdenum plate. The specific heating profile is demonstrated in Figure 1.

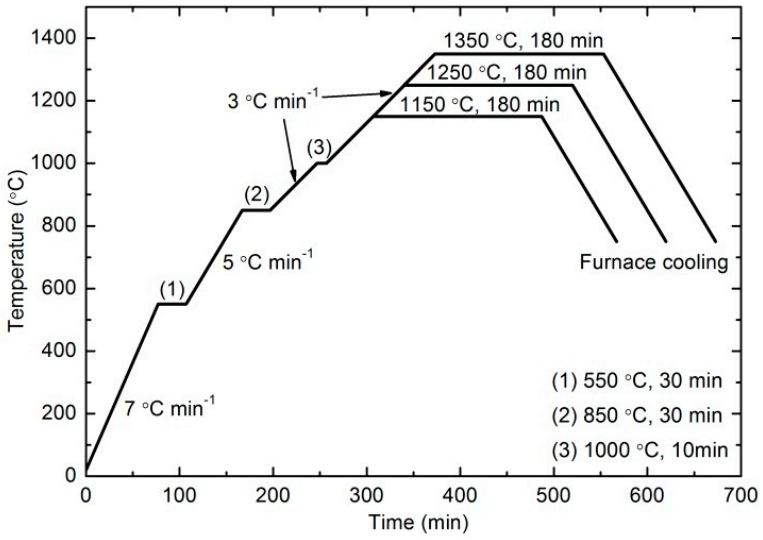

Figure 1. Heating schedule for blended elemental sintered titanium alloys.

The initial heating rate was set at 7 °C·min^{-1} from room temperature to 550 °C. A holding time of 30 min was introduced at both 550 and 850 °C and a 10-min holding time at 1000 °C were used to prevent the possible pore formation caused by the exothermal reaction between titanium and the master alloy or iron powder, and to allow sufficient time for homogeneous elemental diffusion [23]. A slower heating rate of 3–5 °C·min^{-1} was employed from 1000 °C to the final sintering temperature for the same reason.

2.3. Characterization and Mechanical Testing

The particle size distribution was analyzed by a particle size analyzer (Mastersizer 2000, Malvern Instruments, Malvern, UK). The sintered density was measured according to the Archimedes method described in ASTM B962-08. Each data point was averaged from 3–5 specimens. Fine polishing was

conducted with OP-S, a colloidal silica suspension with 10% hydrogen peroxide (H_2O_2), where the size of the colloidal silica is ~40 nm. Microstructural morphology observations were conducted on an environmental scanning electron microscope (ESEM) (Quanta 200F, FEI, Hillsboro, OR, USA) using both back-scattered and secondary electron modes. Semi-quantitative compositional analysis was carried out by energy dispersive spectrometry (EDS, Pegasus detector, EDAX Inc., Mahwah, NJ, USA). Both elemental X-ray mapping and X-ray line scans were carried out using standardless quantification techniques. An accelerating voltage of 20 kV was employed. X-ray diffraction (XRD) analysis to determine phase constituents was carried out on a D2 PHASER (Bruker, Karlsruhe, Germany) equipped with Cu X-ray source. X-ray patterns were collected over a scan range from 2θ of 20–80° with a step size of 0.02°.

Tensile specimens were machined from the sintered specimens in compliance with ISO 2892-1:2009 (~2.65 mm × 2.65 mm cross-section, 15 mm gauge length and 20 mm parallel length), and tested on an Instron mechanical tester (Model: 3367, Instron Co., Norwood, MA, USA) with a crosshead speed of 0.1 mm·min^{-1} (initial strain rate: 1.1 × 10^{-4} s^{-1}). The precise displacement was determined using an extensometer with a gauge length of 8 mm (Model: 2630-120, Instron Co., Norwood, MA, USA). Three tensile specimens were prepared for each data point.

3. Results

3.1. Characteristics of As-Received Powders

The micrographs of as-received powders are shown in Figure 2 including fine titanium, iron and 60Al-40V master alloy powder as well as the particle size distribution of fine titanium and 60Al-40V powders.

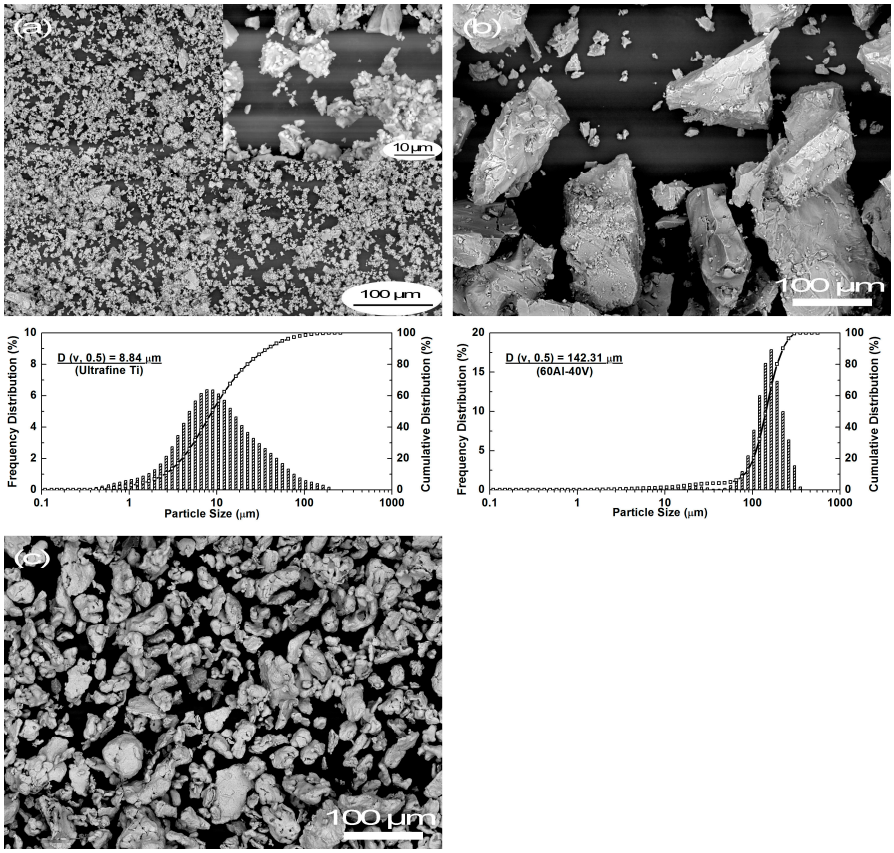

Figure 2. Scanning electron microscope (SEM) images and particle size distribution of (**a**) fine Ti, (**b**) 60Al-40V master alloy and (**c**) Fe powders.

All three powders show angular morphologies, with Figure 2a demonstrating that the fine Ti had a much finer particle size than the 60Al-40V (Figure 2b) and iron (Figure 2c) powders. This was validated by particle size distribution analysis, which illustrates the median particle sizes of fine Ti and master powder were 8.84 and 142.31 μm, respectively. The diameter of most iron particles was less than 50 μm estimated from Figure 2c, which is in accordance with its nominal particle size (−300 mesh). XRD patterns of each powder are given in Figure 3.

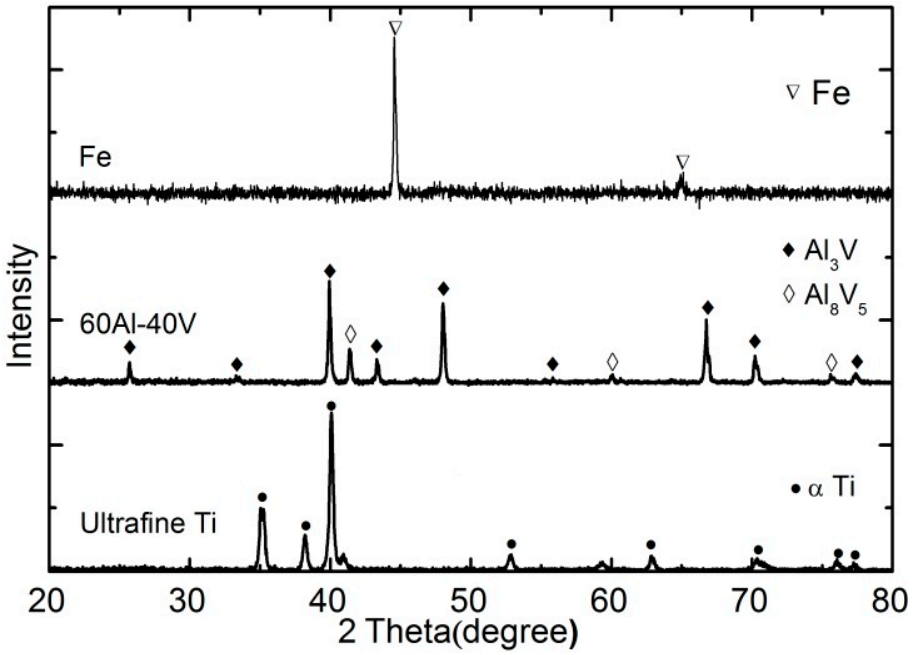

Figure 3. X-ray diffraction (XRD) patterns of as-received powders.

The pattern from the reduced elemental iron powder is indexed as pure iron by JCPDS 87-0721 [24]. The master alloy powder (60Al-40V) is mainly ascribed to Al_3V (JCPDS 07-0399) with a small amount of Al_8V_5 (JCPDS 71-0141) [25]. The fine Ti is mainly composed of α-Ti referenced by JCPDS 44-1294 and some minor titanium oxides.

3.2. Densification

The effect of iron content on the relative sintered density and densification level is illustrated in Figure 4 for specimens uniaxially pressed at a constant compaction pressure of 300 MPa and sintered at different temperatures.

The relative density increases with iron content at sintering temperatures of 1150 and 1250 °C (Figure 4a). However at a sintering temperature of 1350 °C the iron content seems to have little effect on the relative sintered density. As expected, a higher sintering temperature causes an increased sintered density and this effect was more pronounced for the Ti-6Al-4V than for the specimens with Fe. The densification level offers an evaluation method for porosity elimination level of green compacts by sintering. Figure 4b demonstrates that specimens with 6% Fe sintered at 1350 °C have the highest densification level, where ~90% of the porosity of the original green compacts has been eliminated by sintering. The lowest densification level is observed in the Ti-6Al-4V specimens sintered at 1150 °C, where ~20% of the original porosity of the green compacts remains after sintering.

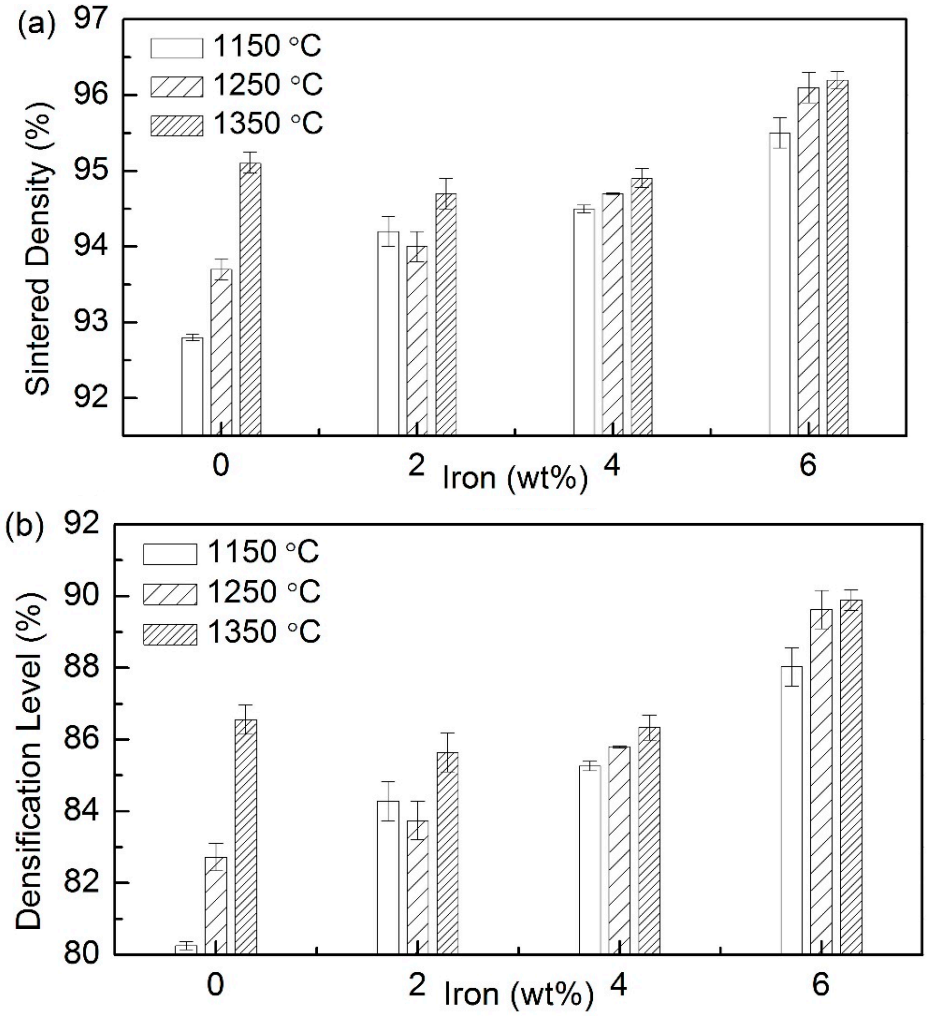

Figure 4. Relative density (**a**) and densification level (**b**) as a function of iron content for samples sintered at different temperatures.

3.3. Microstructure Observation and Compositional Analysis

Microstructural images taken from cross-sections of the specimens sintered at various temperatures and compositions are shown in Figure 5, and confirm the density measurements.

When sintered at temperatures of 1150 and 1250 °C, the porosity decreased with increasing Fe content. At the highest temperature (1350 °C) the relative sintered density of the sample with 2 wt % Fe has the lowest density and the microstructure shows the highest porosity seen in Figure 5(b3). In comparison, the least porosity is observed in the cross-section of the specimen with 6% Fe shown in Figure 5(d3) which has the highest relative sintered density.

Two different types of pores are also observed in Figure 5 in regard to the pore size and shape. Irregular-shaped macropores with an average size of 50–200 μm are noted in all specimens under different sintering temperatures and compositions. The amount of these macropores decreased with the addition of iron content when sintered at either 1150 or 1250 °C. At 1350 °C, a large quantity of irregular-shaped macropores is observed in specimens with 2 wt % Fe. The other type of pores observed is spherical with an average diameter of 5–15 μm. A large number of these micropores are distributed throughout the cross-section of the 1150 °C sintered Ti-6Al-4V, and decreases with increasing sintering temperature. Interestingly, there are only very few micropores observed on the cross-sections of sintered alloys containing iron although their diameter is slightly larger than those in Ti-6Al-4V.

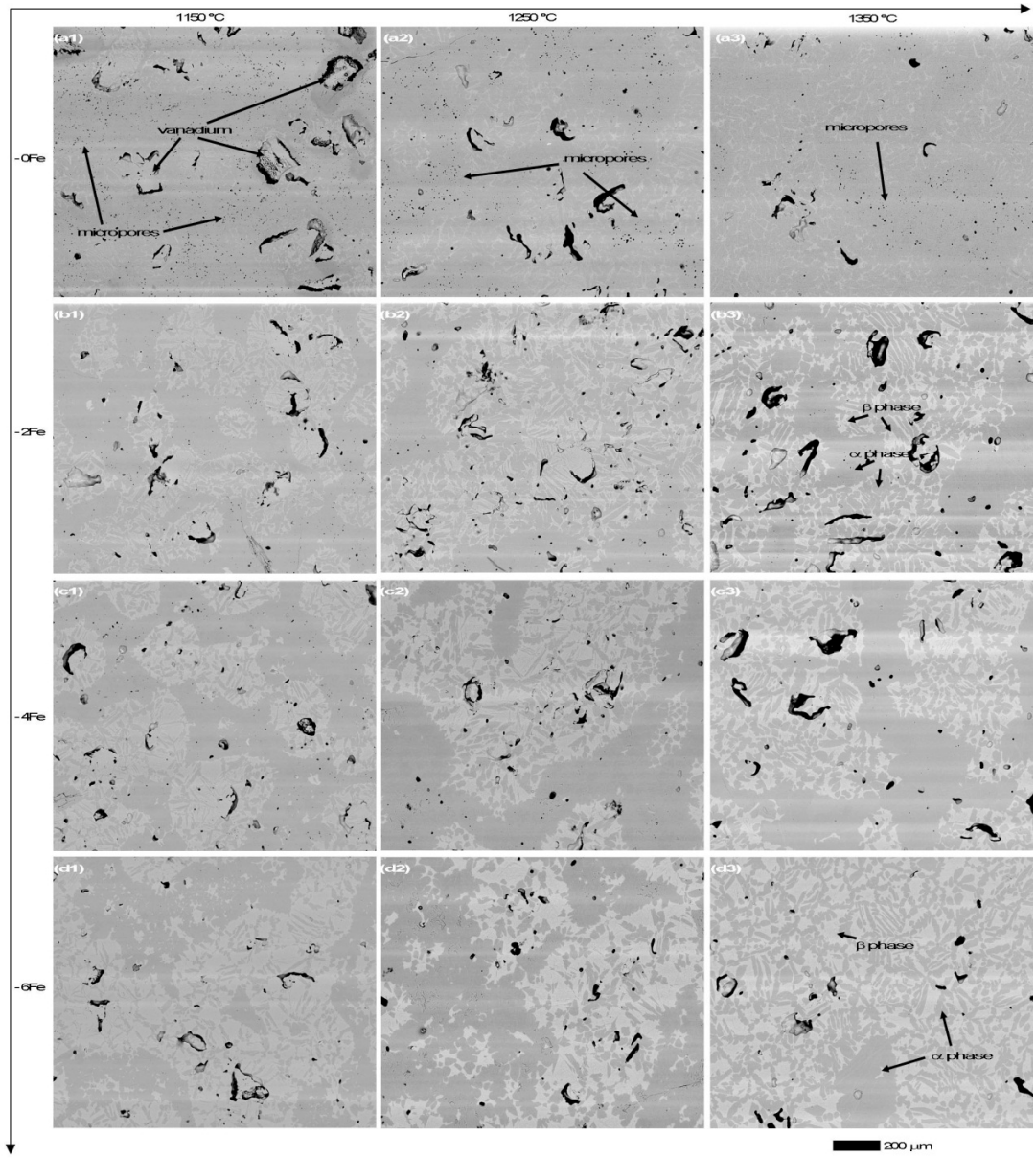

Figure 5. Cross-sectional SEM images of sintered titanium alloys at various temperatures and compositions. The horizontal axis represents the sintering temperature, while the vertical axis represents the iron content.

As also shown in Figure 5, the microstructures show two distinct regions or phases which appear as light and dark contrast in the SEM micrographs, with an increase in the light phase observed with increasing Fe content. It is also observed that the darker contrast regions appear to be in two different morphologies, with smaller needle-like or acicular grains and some much larger particles or grains. In order to further understand these microstructures, compositional analysis was conducted on Ti-6Al-4V sintered at 1150 and 1250 °C including EDS line scanning (Figure 6) and EDS mapping (Figure 7).

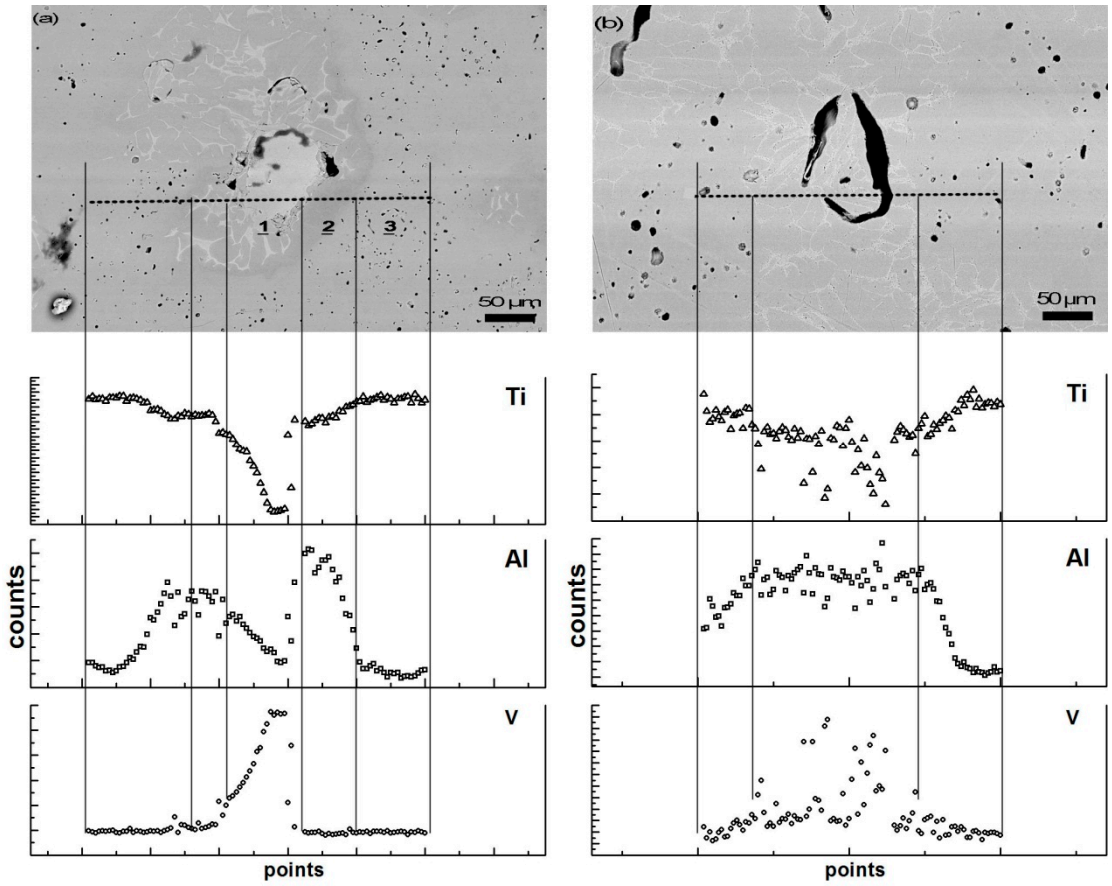

Figure 6. Energy dispersive spectrometry (EDS) line scanning of blended elemental Ti-6Al-4V specimens sintered at (**a**) 1150 °C and (**b**) 1250 °C.

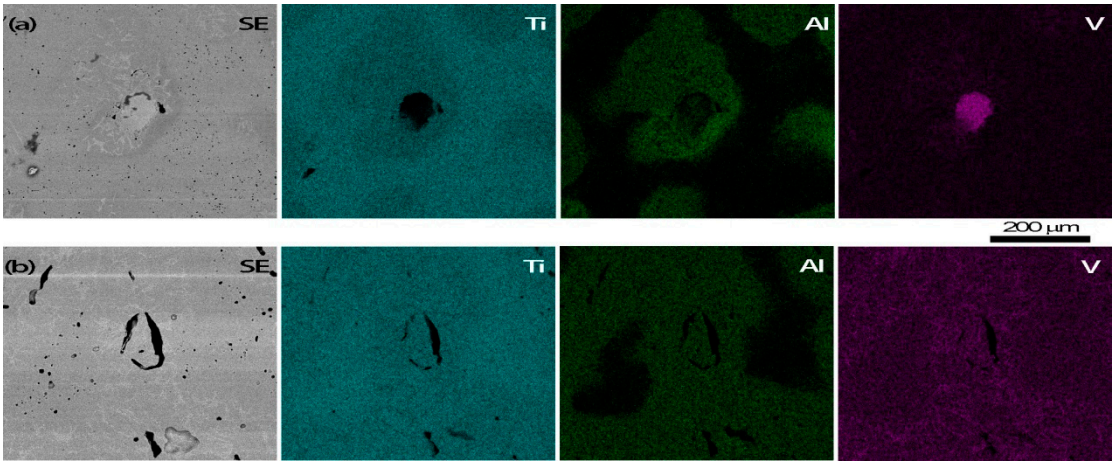

Figure 7. EDS mapping of blended elemental Ti-6Al-4V specimens sintered at (**a**) 1150 °C and (**b**) 1250 °C.

The image in Figure 6 shows a line scan across the area containing the macropores typically seen in the cross-section of Ti-6Al-4V (Figure 5).

For the sample sintered at 1150 °C, the line scan (Figure 6a) is classified into three different regions depending on the color contrast. The light contrast regions (particularly the particle at the center of the pore) are rich in vanadium and contain no Al or Ti. The darkest contrast region around the pore contains both Al and Ti but no V. Moving away from the pore into the mid-contrast, matrix region

there is an increase in the Ti content and a corresponding decrease in Al. The sample sintered at the higher temperature (Figure 6b) shows a much more homogenous distribution of all three elements although vanadium is slightly elevated in the lighter contrast regions.

EDS mapping was also carried out on the same sample to investigate the element distribution as highlighted in Figure 7.

The mapping results are in agreement with the line scanning observation in Figure 6. Figure 7a shows that region 1 is noticeably rich in vanadium whereas region 2 is rich in aluminum. Also, the intensity of titanium decreases gradually from region 3 to region 1 for specimens sintered at 1150 °C. At the higher sintering temperature (Figure 7b), the diffusion area of aluminum became distinctly wider and titanium achieved a more homogeneous elemental distribution when compared with sintering at 1150 °C. A remarkable difference was also witnessed for vanadium, which was no longer isolated in discrete particles but was much more homogeneously distributed. EDS line scanning and mapping of specimens with 4 wt % iron are highlighted in Figure 8 when sintering at the highest temperature (1350 °C).

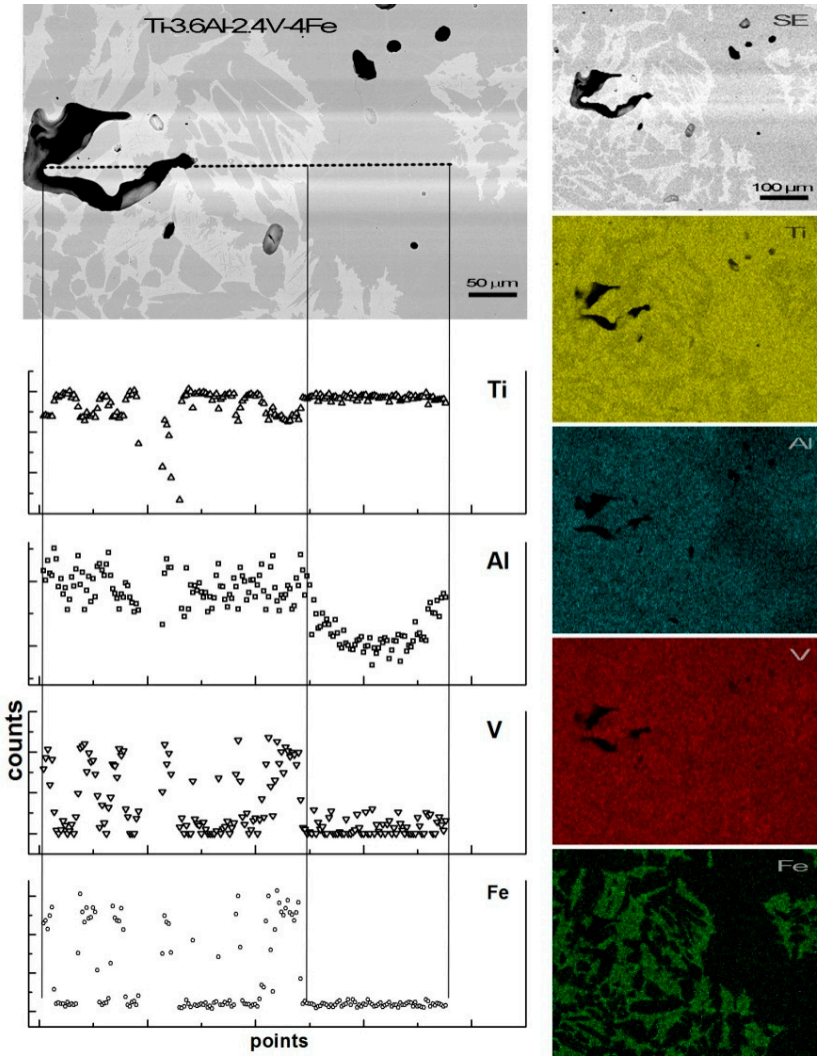

Figure 8. EDS mapping (right column) and EDS line scanning (left column) of Ti-3.6Al-2.4V-4Fe sintered at 1350 °C.

In Figure 8, inhomogeneous microstructural zones can also be distinguished by dark and light contrast regions. It is observed from the corresponding EDS line scanning and mapping that iron is

rich in grains within the light region and is absent in the darker regions. The intensity of aluminum in the blocky darker regions is slightly weaker than those in the lighter contrast areas while the Ti concentration shows the opposite trend, being lower in the lighter regions than in the darker grains. Comparing sintering at the highest temperature (Figure 8) to lower temperatures shown in Figures 6 and 7, improved elemental distribution homogeneity is observed. For example, the contrast of aluminum shown by EDS mapping in Figure 8 is not as strong as shown in Figure 7.

3.4. Phase Determination

The phase analysis of sintered titanium alloys is demonstrated in Figure 9, including the XRD patterns of Ti-6Al-4V sintered under different sintering temperatures (Figure 9a) and the Ti-Al-V-Fe alloys sintered under a constant temperature of 1350 °C (Figure 9b).

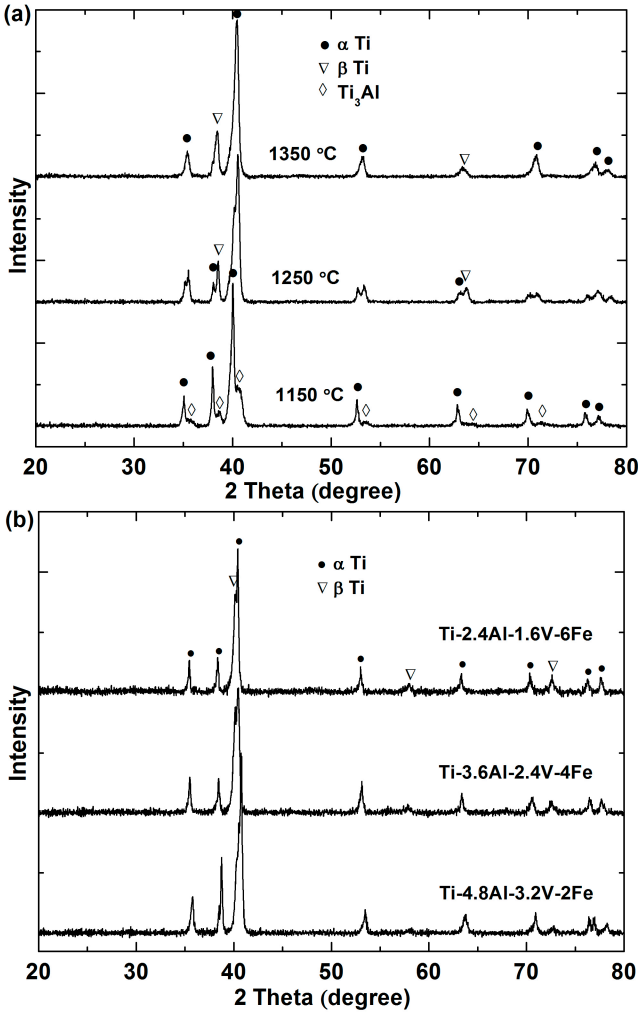

Figure 9. XRD patterns of (**a**) Ti-6Al-4V sintered at various temperatures and (**b**) Ti-Al-V-Fe of various Fe concentrations sintered at 1350 °C.

The XRD patterns of specimens sintered at 1150 °C (Figure 9a), show that the samples consisted of α-, β-Ti with some Ti_3Al peaks [26]. The presence of the Ti_3Al phase when sintered at lower temperatures is indicative of the alloying process being incomplete at these temperatures and supports the microstructural observations. In Figure 9b, peaks attributed to the β-Ti phase are observed for the sintered Ti-Al-V-Fe alloys, as suggested by the literature [19,21], and their intensity increases with increasing iron content in the alloy composition, This indicates that iron stabilizes the β phase in

titanium alloys and more β can be retained after cooling from the sintering temperature if the iron content is increased.

4. Discussion

4.1. Microporosity Formation

Two different types of pores were formed during sintering, which are defined here as micropores (5–15 μm) and macropores (50–200 μm) as shown in Figure 5. The micropores observed in Figure 5 were spherical and isolated in sintered specimens especially in Ti-6Al-4V even at the lowest sintering temperature (1150 °C). Pore spheroidization indicates that sintering had entered into the final stage at this temperature (1150 °C). Although the green density was only about 63% for all of these samples, the sintered density at this lowest temperature was around 93% for the Ti-6Al-4V specimen and increased with increasing iron content up to around 96%. It is considered that the reasonably high levels of densification even at low temperatures and for samples with low green density, as evidenced by the densification results and the presence of isolated small pores, is due mainly to the high sintering driving force resulting from the high surface free energy when using the fine titanium powder, and improved diffusion with the additions of iron.

The evolution of the microporosity for samples with different iron contents as a function of temperature can be seen in the SEM fractographs shown in Figure 10.

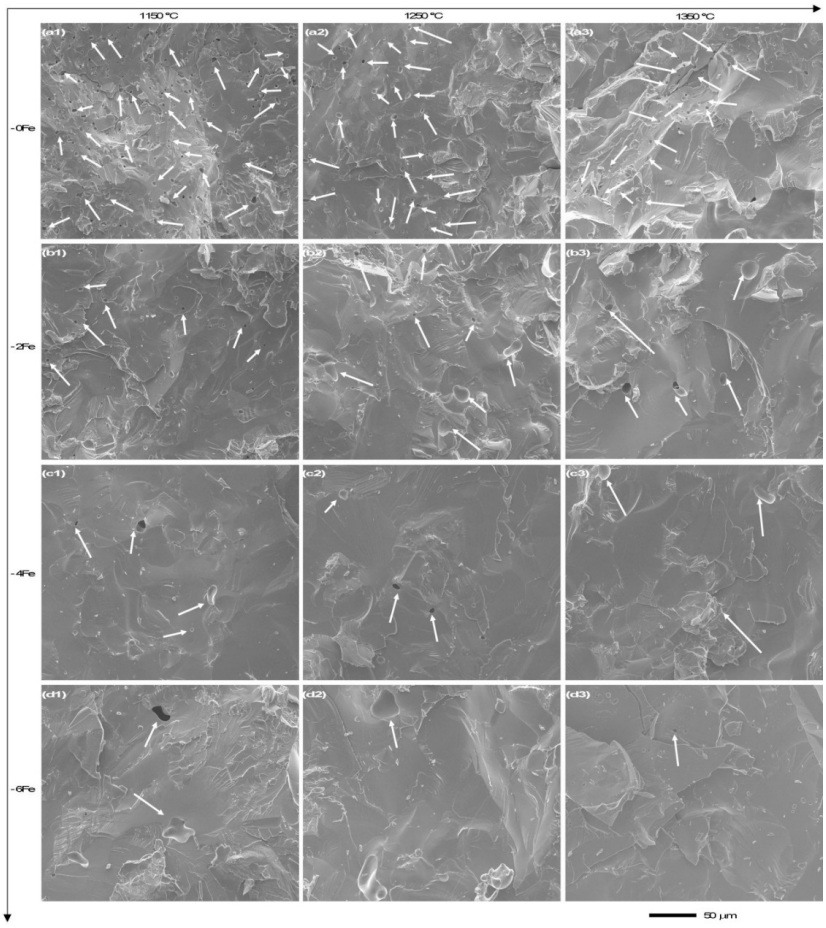

Figure 10. SEM fractographs with micropores of tensile specimens sintered at various temperatures and compositions.

The micropores shown in Figure 10 are in accordance with the observations made from Figure 5, whereby the Ti-6Al-4V specimens show the largest number of micropores (diameter < 10 μm). Although the amount of microporosity in these samples decreased with sintering temperature, the amount of micropores in the Ti-6Al-4V at any temperature was higher than the titanium alloy specimens containing iron. For the Fe containing samples, the microporisity decreased with increasing iron content. This indicates that the addition of iron is beneficial to elimination of micropores; in other words iron assists in densification during sintering.

The diffusion coefficient of elements follows an Arrhenius relationship:

$$D = D_0 \exp(-Q/RT) \quad (3)$$

where D_0 is the pre-exponential factor ($m^2 \cdot s^{-1}$), Q the activation energy ($kJ \cdot mol^{-1}$), R the molar gas constant, and T the absolute temperature (K). These parameters can be obtained for both the self-diffusion of β-Ti and the inter-diffusion of Al, V, and Fe in β-Ti [27] as shown in Table 1.

Table 1. Self-diffusion of β-Ti and inter-diffusion of Al, V, and Fe in β-Ti [27].

Specimen	Diffusion Type	Temperature (°C)	D_0 ($m^2 \cdot s^{-1}$)	Q ($kJ \cdot mol^{-1}$)
β-Ti	Self diffusion	899–1540	3.58×10^{-8}	130.6
Al in β-Ti	Inter-diffusion	920–1600	1.14×10^{-5}	213.1
V in β-Ti	Inter-diffusion	902–1543	3.1×10^{-8}	134.8
Fe in β-Ti	Inter-diffusion	969–1645	7.8×10^{-7}	132.3

Diffusion coefficients were calculated using the data presented in Table 1 and the ratio of inter-diffusion of the different elements to the self-diffusion in Ti are presented in Figure 11 over the temperature range of 1000–1400 °C.

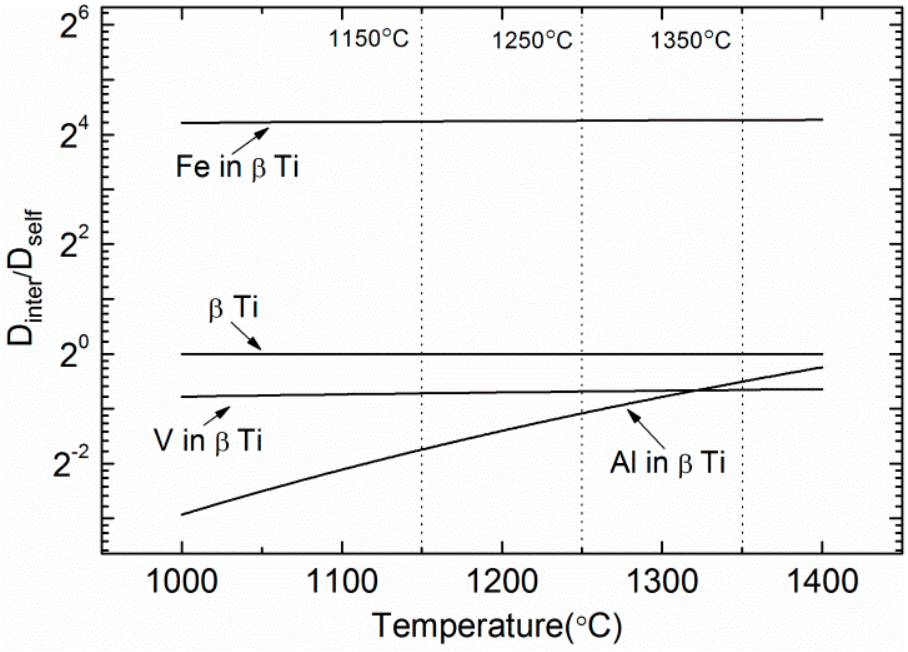

Figure 11. Temperature dependence of ratio of inter-diffusion coefficients to self-diffusion coefficient of β-Ti.

The inter-diffusion coefficient of Fe in β-Ti is over 16 times higher than the self-diffusion coefficient (β-Ti) and is also much higher than the inter-diffusion coefficients of Al and V in Ti (both <1). This indicates that iron is a fast diffuser in β-Ti, and empirical rules of diffusion suggest that the addition of

fast diffusers can enhance self-diffusion rates of both the solute and solvent atoms [28]. Additions of a fast diffuser such as iron can therefore enhance the densification of titanium during sintering.

4.2. Macroporosity Formation

A fractograph of the Ti-6Al-4V sample sintered at 1150 °C is presented in Figure 12 as well as corresponding compositional analyses. Two macropores ~100 µm in diameter are observed in Figure 12, and material with a "coral-like" structure was observed inside the pores. Compositional analysis was conducted on the coral-like material (plot 1) and the more dense surrounding area (plot 2). The EDS spectra and analysis show that the coral-like material was predominantly vanadium (88.78 wt %) whilst the surrounding area was composed of titanium (93.82 wt %) and a small amount of aluminum (3.55 wt %) but no vanadium. The presence of vanadium-rich "coral-like" material with a smooth cellular wall is considered to be correlated with the evaporation of aluminum according to the following analysis.

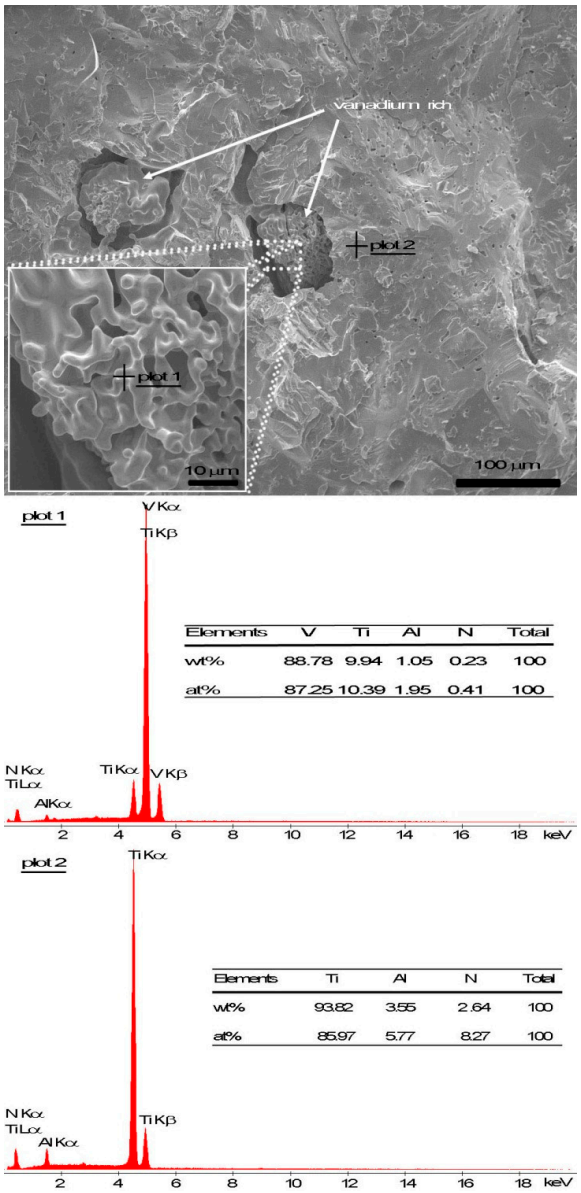

Figure 12. Macropores shown in fracture surface of Ti-6Al-4V specimens sintered at 1150 °C.

Theoretical calculation of the evaporation of binary alloys can be determined based on the Miedema model and Langmuir equation [23,29,30]. For instance, Guo and co-workers calculated the theoretical elemental evaporation of a Ti-Al melt during casting with this model, which had reasonable agreement with the experimental data [29,30]. Chen et al. [23] and Xu et al. [31] also utilized this model to calculate the evaporation of PM fabricated Fe-Al and Fe-Mn alloys in good accordance with experimental observations.

The evaporation loss rate ($N_{m,\,A}$) of the component A in a binary A-B alloy system is demonstrated by the Langmuir theory [29,32]:

$$N_{m,\,A} = \mathrm{K_L} \times \varepsilon \times ({P^e}_A - {P^g}_A) \times \sqrt{M_A/T} \quad (4)$$

The Langmuir constant ($\mathrm{K_L}$) is equal to 4.37×10^{-4} when the partial pressure is described in Pascal [29,30]. ε is the condensation constant (for metals = 1) [29,30]. ${P^e}_A$ indicates the saturated vapor partial pressure of element A in the system and ${P^g}_A$ is the partial pressure of the component. Since the specimens were sintered under high vacuum and the volatiles are reactive with titanium substrate, it is proposed that ${P^g}_A$ can be considered to be zero. M_A and T are the component's atomic mass and absolute temperature respectively.

The saturated vapor partial pressure ${P^e}_A$ can be defined by:

$${P^e}_A = \chi_A \times \gamma_A \times P^0_A \quad (5)$$

where χ_A and γ_A indicate the molar fractions and activity coefficient of component A in the binary system. The equilibrium pressure of pure component A, P^0_A can be calculated for Al and V elements by the following formula [33]:

$$\log_{10} P^0_{\mathrm{Al}} = 14.465 - 17342T^{-1} - 0.7927 \log_{10} T \quad (6)$$

$$\log_{10} P^0_{\mathrm{V}} = 14.75 - 27132T^{-1} - 0.5501 \log_{10} T \quad (7)$$

The activity coefficient of component A (γ_A) in a binary system is given by [34]:

$$\ln \gamma_A = \frac{\Omega}{\mathrm{R}T}(1 - \chi_A)^2 \quad (8)$$

where R is the ideal gas constant and Ω is an interaction parameter which can be obtained by calculating the molar enthalpy of mixing (ΔH_{mix}) for the binary system [34]:

$$\Delta H_{mix} = \Omega \times \chi_A \times \chi_B \quad (9)$$

where χ_A and χ_B are the molar fractions of component A and B respectively.

Substituting Equation (9) into Equation (8), gives:

$$\ln \gamma_B = \frac{\chi_A}{\mathrm{R}T\chi_B}\Delta H_{mix} \quad (10)$$

$$\ln \gamma_A = \frac{\chi_B}{\mathrm{R}T\chi_A}\Delta H_{mix} \quad (11)$$

Thus, the theoretical evaporation loss rate is dependent on the molar enthalpy of mixing (ΔH_{mix}), which can be determined using the model of Miedema [35]:

$$\Delta H_{mix} = \frac{2\mathrm{P}f(c^s)(\chi_A \mathrm{V}_A^{2/3} + \chi_B \mathrm{V}_B^{2/3})}{(\mathrm{n}^{\mathrm{A}}_{\mathrm{ws}})^{-1/3} + (\mathrm{n}^{\mathrm{B}}_{\mathrm{ws}})^{-1/3}} \times \left[-(\varphi_A - \varphi_B)^2 + \frac{\mathrm{Q}}{\mathrm{P}}(\mathrm{n}^{A\ 1/3}_{\mathrm{ws}} - \mathrm{n}^{B\ 1/3}_{\mathrm{ws}})^2 - \mathrm{R/P}\right] \quad (12)$$

where $f(c^s)$ is given by:

$$f(c^s) = f(\chi_A{}^s \chi_B{}^s) = \chi_A \chi_B V_A^{2/3} V_B^{2/3} / (\chi_A V_A^{2/3} + \chi_B V_B^{2/3})^2 \quad (13)$$

$V_A^{2/3}$, $V_B^{2/3}$, $n_{ws}^{A\ 1/3}$, $n_{ws}^{B\ 1/3}$, Q, P, R, φ_A, and φ_B are all constants and are available in the literature [35]. Once the molar enthalpy of mixing is determined, the activity coefficients of Al and V can be calculated from Equations (10) and (11) and combined with the equilibrium pressure (Equations (6) and (7)) to give the saturated vapor pressure (Equation (5)) and ultimately the evaporation rate (Equation (4)).

The weight ratio of Al to V in the 60 wt % Al-40 wt % V master alloy results in an atomic ratio of Al to V of 17:6. Using these values and the model described above, the dependence of the saturated vapor pressure and evaporation rate on temperature is plotted in Figure 13.

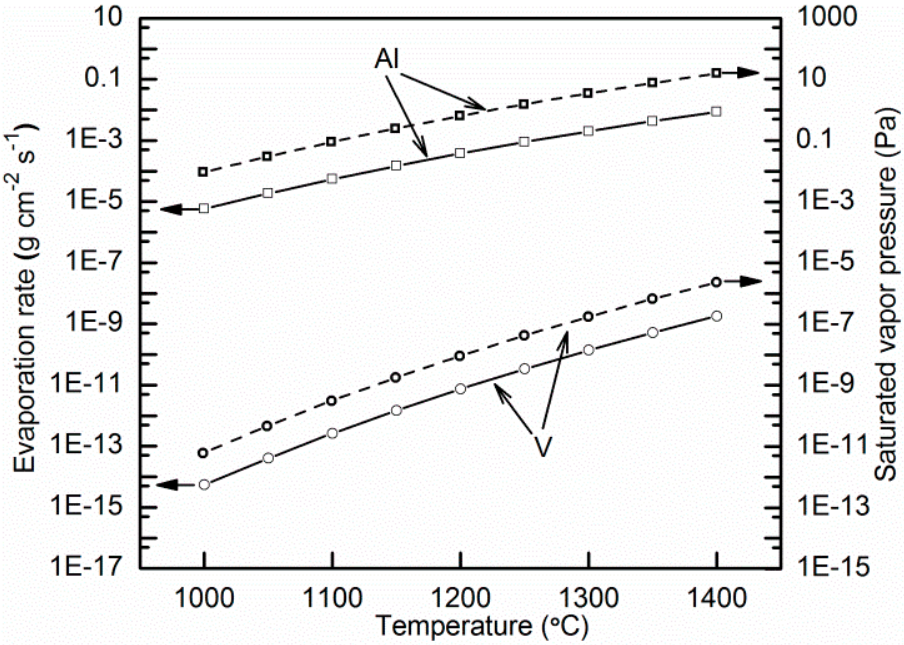

Figure 13. The dependence of evaporation rate and saturated vapor pressure on temperature.

From Figure 13 it can be seen that the saturation vapor pressure of aluminum is 9.2×10^{-3} Pa at a temperature of 1000 °C and increases with temperature. This is higher than the furnace vacuum level of 2×10^{-3} Pa thus suggesting that the Al is in a state of free evaporation [29,30]. The evaporation rate of aluminum and vanadium are 1.48×10^{-4} and 1.48×10^{-12} g·cm^{-2}·s^{-1} respectively at a temperature of 1150 °C seen from Figure 13. The median diameter of the master powder particles was 142.31 µm as shown in Figure 1. Assuming the particle is spherical and the compositional ratio is constant, the mass of aluminum and vanadium in this particle would be 3.15 and 2.1 µg, respectively. When sintering was conducted at the lowest temperature (1150 °C) with a holding time of 3 h, the total loss of aluminum and vanadium by evaporation would be 1.02×10^3 and 1.02×10^{-5} µg respectively. It can be seen that the evaporation loss of aluminum is three orders of magnitude higher than the actual content, whereas, the evaporation of vanadium can be neglected compared with its original mass. This indicates that aluminum had completed the evaporation process before the sintering ends, which is validated by the observation that aluminum is almost non-existent inside the pore shown in Figure 12. It is therefore suggested that the macropores are formed due to the high saturated vapor pressure resulting in the evaporation of aluminum and leaving a vanadium rich region inside the pores whose shape and size are taken from original master particles. These macropores would dramatically decrease both tensile strength and ductility.

4.3. Microstructural Evaluation and Phase Transformation

Haase et al. [25] sintered c.p. Ti powder (<150 μm) blended with a 60Al-40V master powder (<160 μm) prepared by equal-channel angular pressing and the investigation revealed retarded dissolution of master alloy particles due to the formation of Al-rich and V-rich layers, which were assumed to be comprised of intermetallic phases [25]. Therefore, for blended elemental Ti-6Al-4V sintered at 1150 °C shown in Figures 6a and 7a, the phase of region 2 (Figure 6a) can be suggested as α_2-Ti_3Al [36], which is in agreement with the phase determination illustrated in Figure 9a. Moreover, the diffusion of elements in α_2-Ti_3Al is much slower than in β-Ti, for example the diffusion coefficient of Al in β-Ti is almost 2–3 orders of magnitude higher than in α_2-Ti_3Al [36]. Therefore, such intermetallic phase may be considered to be a diffusion barrier for vanadium diffusion which was left by the evaporation of aluminum from the master alloy powders. As indicated by Equation (3) the diffusion coefficient increases with temperature and the intermetallic phases would become no longer stable at higher temperatures (1250 and 1350 °C) compared with 1150 °C. This is in accordance with the observation shown in the literature [25]. Therefore, only α-Ti phase was observed at higher temperature with no intermetallic phase as shown in Figure 9a.

The light region shown in Figure 5 is considered to be β phase because of the abundance of β-stabilizers such as iron and vanadium. The dark region is suggested to be α phase at high temperature (1250 and 1350 °C) including both the blocky regions and acicular grains. Interestingly, the two different "alpha" morphologies are not consistent in composition. In the larger, blocky regions the Al content is much lower and this is thought to be a result of incomplete diffusion of the alloying elements into the Ti matrix because of the distance from the master alloy particle which is the source of aluminum. This is compatible with the unusual microstructural observation.

4.4. Mechanical Properties

Although the microporosity was reduced with the addition of iron, the mechanical properties of these samples were poor: fracture strength in the range of 20 to 100 MPa, with no or little plastic deformation. This is thought to be due to the macroporosity in the sintered samples and high oxygen content in the as-received titanium powders. High oxygen levels in particular are detrimental to the mechanical properties in PM Ti components [4,5,7]. The dependence of oxygen content on median particle size for HDH titanium powder is summarized from the literature [4,37] in Figure 14.

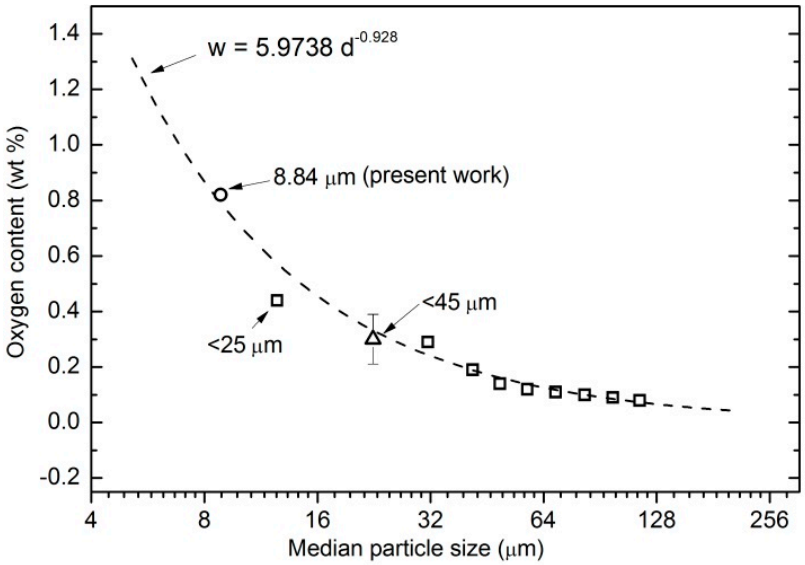

Figure 14. Dependence of oxygen content on median particle size of hydrogenation-dehydrogenation (HDH) titanium powder.

The correlation between oxygen content and median particle size shown in Figure 14 can be expressed by a power-law equation:

$$w = 5.9738\, d^{-0.928} \quad (14)$$

where w is the oxygen content (wt %) and d is the median particle size (μm). The relationship between oxygen content (0.82 wt %) and the median particle size (8.84 μm) of the fine powder used in this work fits well with this relationship. Since oxygen has high solubility in β-Ti [38], the oxygen element, in the form of oxides on titanium particle surfaces, will enter into the β-Ti lattice and therefore, the oxide layer on the titanium particle surface does not affect the densification of blended alloys [5]. However, the oxygen dissolved in β phase would precipitate as oxides at a temperature below the β transus, and these brittle oxides tend to precipitate at grain boundaries. This work has shown that although good densification can be obtained at low temperatures when using the fine titanium powder, the high levels of oxygen impurities results in poor mechanical properties. In order to remedy the poor mechanical properties, the amount of oxides should be reduced and the oxides should not be at the grain boundaries. One strategy is to use an oxygen scavenging element, which has significant solubility in titanium and has more affinity for oxygen than Ti, thus forming non-Ti oxides that are located in the titanium grain interior. Some rare earth elements might serve this purpose [39,40]. Another strategy is to use post-sinter thermomechanical treatments to mechanically move the oxides from grain boundaries to the grain interior.

5. Conclusions

Four different blended elemental titanium alloys were designed and sintered through varying the weight percentage of a fine Ti powder with (Al-V) master alloy and iron powders. Spherical micropores were formed during sintering with fine titanium powder even at the lowest sintering temperature for Ti-6Al-4V. With the addition of Fe, the microporosity was reduced and improved microstructural and compositional homogenization was observed. This is due to fast diffusion of iron in titanium thereby enhancing densification. However, the tensile mechanical properties of these blended elemental titanium alloys were poor with values of <100 MPa tensile strength and almost no elongation. This was mainly caused by high impurity content in the as-received powders and the formation of macropores around the original master alloy particles. Incomplete dissociation of the master alloy particles caused severe evaporation of aluminum resulting in the formation of macropores during sintering.

Although reasonable densification could be obtained with fine titanium powders and this could be improved with the addition of iron, the properties were low because of the high inherent oxygen and macroporosity and therefore special precautions have to be taken when using these powders.

Acknowledgments: This work was supported by Ministry of Business Innovation and Employment (MBIE).

Author Contributions: Changzhou Yu conducted the experimental work as part of his Ph.D. study. He also analyzed the data. Peng Cao and Mark Ian Jones conceived and designed the experiments and analyzed the data. Peng Cao revised the manuscript. Mark Ian Jones discussed the results. Peng Cao and Mark Ian Jones were the supervisors of Changzhou Yu.

Conflicts of Interest: The authors declare no conflict of interest. The founding sponsors had no role in the design of the study; in the collection, analyses, or interpretation of data; in the writing of the manuscript, and in the decision to publish the results.

References

1. German, R.M. *Powder Metallurgy and Particulate Materials Processing*; Metal Powder Industries Federation: Princeton, NJ, USA, 2005.
2. Robertson, I.M.; Schaffer, G.B. Some effects of particle size on the sintering of titanium and a master sintering curve model. *Metall. Mater. Trans. A* **2009**, *40*, 1968–1979. [CrossRef]

3. Luo, S.D.; Yan, M.; Schaffer, G.B.; Qian, M. Sintering of Titanium in Vacuum by Microwave Radiation. *Metall. Mater. Trans. A* **2011**, *42*, 2466–2474. [CrossRef]
4. Robertson, I.M.; Schaffer, G.B. Review of densification of titanium based powder systems in press and sinter processing. *Powder Metall.* **2010**, *53*, 146–162. [CrossRef]
5. Qian, M. Cold compaction and sintering of titanium and its alloys for near-net-shape or preform fabrication. *Int. J. Powder Metall.* **2010**, *46*, 29–44.
6. He, W.; Weng, Q.G.; He, Y.H.; Jiang, Y. Preparation of ultrafine Ti powder by inhibitor coated/HDH combined method. *Powder Metall.* **2013**, *56*, 239–244. [CrossRef]
7. Wang, H.T.; Fang, Z.Z.; Sun, P. A critical review of mechanical properties of powder metallurgy titanium. *Int. J. Powder Metall.* **2010**, *46*, 45–57.
8. Geetha, M.; Singh, A.K.; Asokamani, R.; Gogia, A.K. Ti based biomaterials, the ultimate choice for orthopaedic implants—A review. *Prog. Mater. Sci.* **2009**, *54*, 397–425. [CrossRef]
9. Ivasishin, O.M.; Savvakin, D.G.; Froes, F.; Mokson, V.C.; Bondareva, K.A. Synthesis of alloy Ti-6Al-4V with low residual porosity by a powder metallurgy method. *Powder Metall. Met. Ceram.* **2002**, *41*, 382–390. [CrossRef]
10. Peter, W.; Chen, W.; Yamamoto, Y.; Dehoff, R.; Muth, T.; Nunn, S.; Kiggans, J.; Clark, M.; Sabau, A.; Gorti, S.; et al. Current Status of Ti PM: Progress, Opportunities and Challenges. *Key Eng. Mater.* **2012**, *520*, 1–7. [CrossRef]
11. Bolzoni, L.; Ruiz-Navas, E.M.; Gordo, E. Understanding the properties of low-cost iron-containing powder metallurgy titanium alloys. *Mater. Des.* **2016**, *110*, 317–323. [CrossRef]
12. Bolzoni, L.; Ruiz-Navas, E.M.; Gordo, E. Quantifying the properties of low-cost powder metallurgy titanium alloys. *Mater. Sci. Eng. A* **2017**, *687*, 47–53. [CrossRef]
13. Wei, W.; Liu, Y.; Zhou, K.; Huang, B. Effect of Fe addition on sintering behaviour of titanium powder. *Powder Metall.* **2003**, *46*, 246–250. [CrossRef]
14. Savvakin, D.G.; Carman, A.; Ivasishin, O.M.; Matviychuk, M.V.; Gazder, A.A.; Pereloma, E.V. Effect of Iron Content on Sintering Behavior of Ti-V-Fe-Al Near-beta Titanium Alloy. *Metall. Mater. Trans. A* **2012**, *43*, 716–723. [CrossRef]
15. Qian, M.; Yang, Y.F.; Yan, M.; Luo, S.D. Design of low cost high performance powder metallurgy titanium alloys: Some basic considerations. *Key Eng. Mater.* **2012**, *520*, 24–29. [CrossRef]
16. Esteban, P.G.; Ruiz-Navas, E.M.; Bolzoni, L.; Gordo, E. Low-cost titanium alloys? Iron may hold the answers. *Met. Powder Rep.* **2008**, *63*, 24–27. [CrossRef]
17. Liu, Y.; Chen, L.F.; Tang, H.P.; Liu, C.T.; Liu, B.; Huang, B.Y. Design of powder metallurgy titanium alloys and composites. *Mater. Sci. Eng. A* **2006**, *418*, 25–35. [CrossRef]
18. Carman, A.; Zhang, L.C.; Ivasishin, O.M.; Savvakin, D.G.; Matviychuk, M.V.; Pereloma, E.V. Role of alloying elements in microstructure evolution and alloying elements behaviour during sintering of a near-beta titanium alloy. *Mater. Sci. Eng. A* **2011**, *528*, 1686–1693. [CrossRef]
19. Yang, Y.F.; Luo, S.D.; Schaffer, G.B.; Qian, M. Sintering of Ti-10V-2Fe-3Al and mechanical properties. *Mater. Sci. Eng. A* **2011**, *528*, 6719–6726. [CrossRef]
20. Esteban, P.G.; Ruiz-Navas, E.M.; Gordo, E. Influence of Fe content and particle size the on the processing and mechanical properties of low-cost Ti-xFe alloys. *Mater. Sci. Eng. A* **2010**, *527*, 5664–5669. [CrossRef]
21. Chen, B.Y.; Hwang, K.S.; Ng, K.L. Effect of cooling process on the alpha phase formation and mechanical properties of sintered Ti-Fe alloys. *Mater. Sci. Eng. A* **2011**, *528*, 4556–4563. [CrossRef]
22. Yang, Y.F.; Luo, S.D.; Schaffer, G.B.; Qian, M. The Sintering, Sintered Microstructure and Mechanical Properties of Ti-Fe-Si Alloys. *Metall. Mater. Trans. A* **2012**, *43A*, 4896–4906. [CrossRef]
23. Chen, G.; Cao, P.; He, Y.H.; Shen, P.Z.; Gao, H.Y. Effect of aluminium evaporation loss on pore characteristics of porous FeAl alloys produced by vacuum sintering. *J. Mater. Sci.* **2012**, *47*, 1244–1250. [CrossRef]
24. Kang, K.S.; Kim, C.H.; Cho, W.C.; Bae, K.K.; Woo, S.W.; Park, C.S. Reduction characteristics of $CuFe_2O_4$ and Fe_3O_4 by methane; $CuFe_2O_4$ as an oxidant for two-step thermochemical methane reforming. *Int. J. Hydrogen Energy* **2008**, *33*, 4560–4568. [CrossRef]
25. Haase, C.; Lapovok, R.; Ng, H.P.; Estrin, Y. Production of Ti-6Al-4V billet through compaction of blended elemental powders by equal-channel angular pressing. *Mater. Sci. Eng. A* **2012**, *550*, 263–272. [CrossRef]

26. Bolzoni, L.; Esteban, P.G.; Ruiz-Navas, E.M.; Gordo, E. Mechanical behaviour of pressed and sintered titanium alloys obtained from prealloyed and blended elemental powders. *J. Mech. Behav. Biomed. Mater.* **2012**, *14*, 29–38. [CrossRef] [PubMed]
27. Neumann, G.; Tuijn, C. *Self-Diffusion and Impurity Diffusion in Pure Metals: Handbook of Experimental Data*; Elservier: Amsterdam, The Netherlands, 2008; Volume 14, pp. 1–349.
28. Yang, Y.F.; Luo, S.D.; Bettles, C.J.; Schaffer, G.B.; Qian, M. The effect of Si additions on the sintering and sintered microstructure and mechanical properties of Ti-3Ni alloy. *Mater. Sci. Eng. A* **2011**, *528*, 7381–7387. [CrossRef]
29. Su, Y.Q.; Guo, J.J.; Jia, J.; Liu, G.Z.; Liu, Y.A. Composition control of a TiAl melt during the induction skull melting (ISM) process. *J. Alloys Compd.* **2002**, *334*, 261–266.
30. Guo, J.J.; Liu, Y.; Su, Y.Q.; Ding, H.S.; Liu, G.Z.; Jia, J. Evaporation behavior of aluminum during the cold crucible induction skull melting of titanium aluminum alloys. *Metall. Mater. Trans. B* **2000**, *31B*, 837–844. [CrossRef]
31. Xu, Z.; Hodgson, M.A.; Chang, K.; Chen, G.; Yuan, X.; Cao, P. Effect of Sintering Time on the Densification, Microstructure, Weight Loss and Tensile Properties of a Powder Metallurgical Fe-Mn-Si Alloy. *Metals* **2017**, *7*, 81. [CrossRef]
32. Langmuir, I. The Vapor Pressure of Metallic Tungsten. *Phys. Rev.* **1913**, *2*, 329–342. [CrossRef]
33. Alcock, C.B. Vapor pressure of the metallic elements—Equations. In *CRC Handbook of Chemistry and Physics (Internet Version 2013)*, 93rd ed.; Haynes, W.M., Ed.; CRC Press: Boca Raton, FL, USA, 2013; pp. 125–126.
34. Porter, D.A.; Easterling, K.E.; Sherif, M.Y. *Phase Transformations in Metals and Alloys*, 3rd ed.; CRC Press: Boca Raton, FL, USA, 2009.
35. Miedema, A.R.; de Chatel, P.F.; de Boer, F.R. Cohesion in alloys—Fundamentals of a semi-empirical model. *Physica B* **1980**, *100*, 1–28. [CrossRef]
36. Mishin, Y.; Herzig, C. Diffusion in the Ti-Al system. *Acta Mater.* **2000**, *48*, 589–623. [CrossRef]
37. McCracken, C. Production of Fine Titanium Powders via the Hydrid-Dehydride (HDH) Process. *PIM Int.* **2008**, *2*, 55–57.
38. Massalski, T.D. *Binary Alloys Phase Diagams*; Okamoto, H., Subramanian, P.R., Kasprzak, L., Eds.; ASM International: Geauga County, OH, USA, 1990.
39. Yan, M.; Liu, Y.; Liu, Y.B.; Kong, C.; Schaffer, G.B.; Qian, M. Simultaneous gettering of oxygen and chlorine and homogenization of the beta phase by rare earth hydride additions to a powder metallurgy Ti-2.25Mo-1.5Fe alloy. *Scr. Mater.* **2012**, *67*, 491–494. [CrossRef]
40. Luo, S.D.; Yang, Y.F.; Schaffer, G.B.; Qian, M. The effect of a small addition of boron on the sintering densification, microstructure and mechanical properties of powder metallurgy Ti-7Ni alloy. *J. Alloys Compd.* **2013**, *555*, 339–346. [CrossRef]